Energy & Environmental Science

ROYAL SOCIETY OF CHEMISTRY

PAPER

View Article Online
View Journal

Cite this: DOI: 10.1039/d6ee01118g

Direct electrode-to-electrode regeneration of end-of-life batteries *via* electrode–electrolyte interphase dissolution

Kiwon Kim,[a] Chenlu Yang,[b] Sabine M. Gallagher,[c] Shuwen Yue [a] and Vibha Kalra *[a]

Received 17th February 2026,
Accepted 20th May 2026

DOI: 10.1039/d6ee01118g

rsc.li/ees

Lithium-ion battery recycling remains constrained by processes that recover metals at the expense of electrode integrity, while even direct recycling typically requires shredding to black mass followed by binder removal, separation, and full electrode refabrication. Here, we introduce direct electrode-to-electrode regeneration (DEER), a simultaneous electrochemical regeneration of used NMC and graphite electrodes from end-of-life batteries in their intact form by dissolving the passivating electrode–electrolyte interphase (EEI). DEER employs 1,3-dimethyl-2-imidazolidinone (DMI), a high donor number solvent that creates a thermodynamic environment favorable for solubilizing redox inactive EEI components. DEER dissolves the thick EEI on both used electrodes while preserving electrode integrity, enabling up to 95% capacity regain and improved cycling stability with a residual LiF-rich interphase. *Operando* Raman, *operando* IR, and post-mortem NMR directly track the electrochemically driven dissolution of carbonate-derived EEI species in the used DMI-based recycling electrolyte. Technoeconomic and life-cycle analyses show that DEER reduces the cost of recycled cell manufacturing by 56% relative to pyro- and hydrometallurgy, while lowering energy use and greenhouse gas emissions. Overall, DEER establishes the first validated pathway to directly regenerate and reuse electrodes harvested from truly end-of-life batteries, converting the key interfacial bottleneck into a controllable dissolution process and opening a practical route toward electrode level circularity.

Broader context

The rapid deployment of lithium-ion batteries for electric vehicles and grid storage intensifies the need for recycling strategies that can shorten the recycling loop while reducing energy use and environmental burdens. Direct recycling approaches that rejuvenate spent cathode materials have therefore gained attention as a pathway toward more sustainable battery circularity. However, most strategies are developed on reprocessed powders and remain fundamentally constrained because of requirements for electrode refabrication and battery remanufacturing. In practical batteries, the accumulation of electrochemically inactive electrode–electrolyte interphase layers suppresses ion transport and interfacial redox reactions, imposing a primary bottleneck for cathode and anode regeneration. By reframing the electrode–electrolyte interphase as the primary, addressable bottleneck for electrode reuse, this work establishes interphase engineering as a foundational design principle for battery recycling. This electrode-level regeneration framework provides a scalable pathway toward closed-loop battery manufacturing with substantially reduced cost, energy consumption, and greenhouse gas emissions, supporting more sustainable electrification at the system level.

Introduction

As lithium-ion batteries (LIB) emerge as the backbone of transportation and energy storage, their exponential growth highlights the urgent need for sustainable end-of-life (EOL) management.[1,2] Conventional recycling methods, such as pyrometallurgy and hydrometallurgy, rely on energy-intensive smelting, and toxic leaching agents, resulting in hazardous waste.[3,4] In addition, both approaches irreversibly convert battery active materials into metal alloys or salts of LiOH, Li_2CO_3, and metal sulfates.[5,6] In response, direct battery recycling offers promising strategies to minimize active material resynthesis and shorten the battery recycling loop.[7,8] Most direct recycling approaches focus either on structural reconstruction or on relithiation of spent active materials such as NMC, LCO,

[a] Smith School of Chemical and Biomolecular Engineering, Cornell University, Ithaca, New York 14853, USA. E-mail: vk69@cornell.edu
[b] Department of Chemistry and Chemical Biology, Cornell University, Ithaca, New York, 14853, USA
[c] Applied Materials Division, Argonne National Laboratory, Lemont, Illinois, 60439, USA

and graphite.[9–11] For instance, structural restoration and lithium replenishment have been achieved through LiCoMnBO surface coatings or fluorenone-mediated lithiation of spent cathode powder, followed by annealing above 800 °C.[7,12] While these strategies have effectively restored active materials without the need for resynthesis, they still rely on producing black mass powder by shredding batteries, followed by the removal of binders and conductivity agents and the complicated separation of cathode and anode active materials. The recycled active materials must then re-enter conventional electrode manufacturing steps such as slurry mixing, coating, drying, and slitting before cell assembly, which account for up to 42% of the manufacturing cost and 57% of the energy consumption in the production of 32-Ah lithium-ion batteries.[13] The resulting economical and logistical barriers to practical battery recycling remains far from ideal.

A few groups have simulated lithium-deficient cells by limiting the state of charge and regenerated electrodes without disassembly or dismantling by replenishing lithium using redox active chemical species such as Li naphthalene complexes or 5,10-dimethylphenazine.[14,15] These strategies successfully restored a substantial portion of the electrode capacity up to the initial performance, highlighting the conceptual feasibility of electrode regeneration as an alternative to powder-based direct recycling. However, these demonstrations were carried out on idealized systems with the assumption that the electrode surface remained accessible and chemically active. Electrodes harvested from end-of-life cells differ fundamentally from these idealized, simulated lithium deficient systems.[16,17] After a few hundred to a few thousand battery cycles under real operating conditions, practical cells undergo a complex set of degradation pathways, including electrolyte decomposition, parasitic reactions, structural distortions, and transition metal dissolution.[16,18] A particularly critical outcome is the continuous growth and accumulation of the electrode–electrolyte interphase (EEI) layer on both the cathode and anode.[19,20] This aged EEI becomes a thick, resistive, and chemically heterogeneous layer that suppresses ion transport and interfacial charge transfer, while promoting parasitic chemistry.[21,22] Because all lithium replenishment and redox-mediated repair reactions operate through the surface of active materials, a thick and resistive EEI can block the chemical reaction for battery recycling, making electrode regeneration fundamentally impossible without first removing the aged EEI layers.[23,24] Moreover, recent studies on the diagnosis of battery degradation indicate that, up to a state of health of nearly 80%, performance degradation is dominated not by structural collapse or irreversible lithium loss but rather by EEI-layer-driven impedance growth.[17] Even though the EEI may be the primary barrier to the regeneration of electrodes, no existing battery recycling approach directly targets its removal or reconstruction, revealing a critical gap in current electrode-level recycling. An EEI-targeted strategy would not only enable practical implementation of lithium replenishment concepts but also allow degraded electrodes to be regenerated in their intact form while remaining coated on the current collector.

Motivated by this gap, our work starts from the hypothesis that the accumulated EEI on both the cathode and anode is a primary bottleneck for electrode-level regeneration. We introduce an electrochemical direct electrode-to-electrode regeneration (DEER) process in which EEI layers on the cathode and anode are dissolved through electrochemical activation in 1,3-dimethyl-2-imidazolidinone (DMI), a solvent with a high donor number (DN). DMI, characterized by its strong electron-donating capability and elevated molecular orbital energy levels, creates a thermodynamic environment that selectively dissolves redox-inactive EEI components. DEER completely removes inactive EEI layers and simultaneously regenerates both NMC and graphite that perform comparably to pristine ones, while preserving the structural and electrochemical integrity of the electrodes. DEER restores the capacity of a regenerated electrode up to 95% of its initial capacity and delivers enhanced cycle stability beyond that of the original cell, supported by the thin remaining LiF components. *Operando* Raman, IR (infrared), and NMR analyses further confirm that the interphase dissolution occurs through an electrochemical pathway due to the favorable thermodynamic environment derived by the high donicity of DMI. Technoeconomic and life-cycle assessments show that, despite a modest cost for DMI, DEER delivers higher recycling profits for processing end-of-life batteries and lower cost for producing recycled batteries with substantially lower energy use, greenhouse gas emissions than conventional pyro- and hydrometallurgy. In contrast to previous direct battery recycling approaches that rely on structural reconstruction or lithium replenishment, DEER is the first validated strategy to reactivate degraded electrodes through EEI dissolution-driven regeneration, eliminating the need for material breakdown, resynthesis, and electrode refabrication. Building on this capability, DEER demonstrates a shortened and practical recycling loop that aligns with a feasible battery roadmap and delivers both economic and environmental benefits.

Results and discussion

To explore electrochemical direct regeneration *via* electrode–electrolyte interphase (EEI) layer dissolution, we use end-of-life (EOL) lithium-ion batteries exhibiting less than 80% of their original capacity. The batteries were fabricated with NMC85:05:10 cathodes and graphite (Gr) anodes. The EEI layer collectively refers to the solid electrolyte interphase (SEI) and cathode electrolyte interphase (CEI) formed on the anode and cathode, respectively, and originates from the decomposition of carbonate-based electrolytes and $LiPF_6$, producing a complex mixture of Li-organic and Li-inorganic species.[25,26] Here, the EEI layer collectively refers to the solid electrolyte interphase (SEI) and cathode electrolyte interphase (CEI) formed on the anode and cathode, respectively, which originate from the decomposition of carbonate-based electrolytes and LiPF6, producing a complex mixture of Li-organic and Li-inorganic species. Although EEI layers initially contribute to electrode stabilization, they can grow excessively or become electrochemically inactive during prolonged cycling, eventually passivating the electrode surface, hindering Li^+ transport, and reducing the reversibility of the electrochemical

reactions.[27] To address this challenge, we developed an electrochemical DEER strategy in which the degraded cathode and anode are separated from EOL batteries and both electrodes are simultaneously electrochemically regenerated in a high DN electrolyte. DN, introduced by Gutmann, is a quantitative Lewis basicity scale defined by the enthalpy of 1 : 1 adduct formation between a solvent and $SbCl_5$.[28] In battery interphases, a higher DN can strengthen solvent interactions with Li containing organic and inorganic EEI species, thereby modulating their solubility, binding strength, and dissolution equilibrium.[29,30] Here, electrode regeneration refers to recycling and reuse of electrodes in their intact form, serving as a concept distinct from the previous powder-based direct recycling. Then, the DEER treatment induces dissolution of the inactive EEI layers on the cathode and anode at the same time. Finally, the regenerated electrodes are reassembled into new cells (Fig. 1a).

To dissolve accumulated EEI species that cannot be dissolved by conventional carbonate electrolytes, DMI was selected as the recycling solvent for DEER. Compared with the carbonate electrolyte of EC or DEC, DMI contains N atoms in its molecular structure (Fig. S1) and exhibits favorable physicochemical and electrochemical characteristics, including moderate viscosity (1.9 C_P at 25 °C), a low melting point (8.2 °C), a high boiling point (225 °C), and excellent oxidative stability (up to 4.3 V *vs.* Li/Li^+) (Fig. S2).[31] Along with these properties, the occupational health, safety, and environment (OHSE) aspects of using DMI support handling comparable to those of conventional battery electrolyte solvents (Note S1). Additionally, DMI exhibits a high donor number (29.0 kcal mol^{-1}), which enables strong electron donation to EEI species and promotes their chemical/electrochemical dissociation (Fig. S3).[32] This value is higher than those of other well-known battery electrolyte solvents, such as FEC (15.1), DEC (16.5), EC (17.3), DOL (21.3), and DME (20.1).[31,33,34] Moreover, DMI also possesses a high dielectric constant (37.6 at 25 °C), which can potentially promote dissolution of EEI components as ionic compounds by stabilizing the resulting charged species with strong solvation structures.[31] To clarify how theoretically DMI promotes EEI dissolution during DEER, density functional theory (DFT) calculations were performed to determine the highest occupied molecular orbital (HOMO) and lowest unoccupied molecular orbital (LUMO) energy levels of DMI and other representative solvents (Fig. 1b). The highest HOMO energy of DMI indicates that it

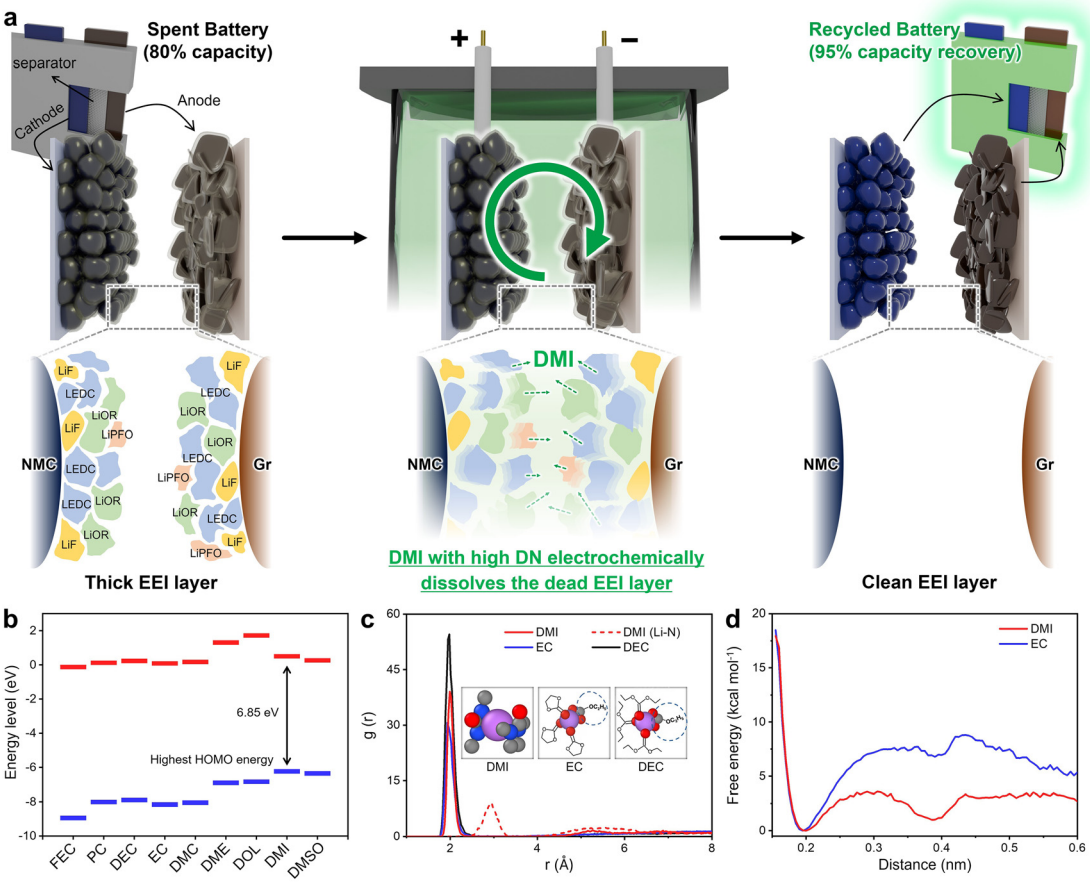

Fig. 1 (a) Schematic diagram of SEI/CEI layer dissolution for direct battery recycling. (b) Calculated HOMO and LUMO energy levels of FEC, PC, DEC, EC, DMC, DME, DOL, DMI, and DMSO. (c) Radial distribution functions, $g(r)$, between Li^+ from the organic EEI component of $LiOCO_2C_2H_5$ and coordinating solvent atoms in EC, DEC, and DMI. The blue dotted line circles highlight the Li^+ ion that remains associated with the SEI fragments in EC and DEC, in contrast to the fully dissociated Li^+ observed in DMI. (d) Free-energy evaluation along the Li–O separation between the Li^+ and the organic EEI component $LiOCO_2C_2H_5$ in EC and DMI.

is more likely to donate electrons, especially near the local region of the EEI layer at the electrode surface.[34,35] In contrast, the elevated LUMO level compared to other solvents reduces the propensity for reductive decomposition at the electrode, preventing new EEI formation during DEER.[36] As a result, the theoretical electronic structure of DMI neither induces parasitic reactions nor promotes the formation of new EEI layers during DEER. Further molecular-level insights into EEI dissolution were obtained from force-field-based molecular dynamics simulations. In EC and DEC solvents, Li^+ remains associated with the organic EEI fragment of $OCO_2C_2H_5^-$ and is solvated by only three carbonyl oxygen atoms in the surrounding solvent (Fig. 1c and Table S1). In contrast, DMI enables full dissociation of Li^+ from $OCO_2C_2H_5^-$ by stabilizing a dense mixed-donor shell composed of four nitrogen atoms and two carbonyl oxygen atoms, resulting in a broader, multi-site and more densely populated solvation structure than in EC or DEC. In addition, the DMI solvated system exhibits a reduced free energy penalty for separating Li^+ and the organic fragment, which is consistent with enhanced stabilization of the dissociated configurations (Fig. 1d). This enhanced solvation environment in DMI suggests the potential for more effective dissolution of EEI species compared to EC and DEC, conventional battery electrolyte solvents.

To validate the effectiveness of DEER with EEI layer dissolution in a high DN solution environment, various electrochemical protocols and solvents with different DNs were evaluated for their ability to regenerate end-of-life NMC/Gr cells at 80% of their initial capacity (Fig. S4–S6). Here, R-NMC and R-Gr denote the NMC and graphite regenerated by DEER in the DMI recycling electrolyte, while D-NMC and D-Gr denote degraded NMC and graphite taken from spent NMC/Gr cells. R-NMC/Gr refers to a reassembled cell with R-NMC and R-Gr after simultaneous DEER treatment of D-NMC and D-Gr in DMI, while D-NMC/Gr refers to a reassembled cell with D-NMC and D-Gr. To minimize cell-to-cell variability in evaluating DEER, only D-NMC/Gr cells exhibiting less than 3% capacity variation prior to disassembly were used (Fig. S7). Although DMSO with a DN of 29.8 showed EEI dissolution capability comparable to that of DMI with a DN of 28 (Fig. S8), it also induced parasitic degradation of the graphite lattice and PVDF binder, resulting in poor capacity recovery (Fig. S9). These results support the role of DN in facilitating EEI dissolution, while demonstrating that accurate prediction of DEER solvent performance requires an integrated assessment of electrochemical stability, HOMO/LUMO levels, dielectric constant, viscosity, solvation structure, and electrode compatibility. Note S2 provides a detailed explanation and comparison of the different protocols tested. The regained capacity of regenerated electrodes serves as the primary metric for evaluating various recycling protocols and electrolytes for DEER. Among these, cyclic voltammetry (CV) scanning within the voltage window of 3.0–4.1 V *vs.* Li/Li^+ proved most effective for recovering the capacity of degraded electrodes from spent NMC/Gr cells (Fig. 2a). While discharge/charge cycling induces bulk redox reactions, CV scans promote surface reactions with minimal side reactions, making them particularly favorable for EEI layer dissolution. Furthermore, during the regeneration CV scan, the current density is reduced by 40% and 20%, respectively, at the 2nd and 3rd scans than that of the initial scan, indicating the progressive removal of EEI species that were previously redox inactive in spent NMC/Gr cells with the carbonate electrolyte. The resistance changes during DEER are monitored using electrochemical impedance spectroscopy (EIS) after each CV scan (Fig. 2b and c). Notably, after three CV scans, the Nyquist plot of the cell using degraded NMC/degraded graphite closely resembled that of the pristine NMC/Gr, and equivalent circuit fitting revealed a progressive decrease in the resistance of the EEI (R_{EEI}). In contrast, the series resistance of R_s increases slightly possibly due to the accumulation of dissolved EEI components in the electrolyte, which increases the internal resistance.[37] So R-NMC and R-Gr are defined as the D-NMC and D-Gr regenerated by DEER after completing the 3rd regeneration scan in DMI electrolytes. To further examine the chemical evolution of the electrode surfaces, X-ray photoelectron spectroscopy (XPS) was performed before and after DEER (Fig. 2d). Both original and deconvoluted XPS spectra are provided in Fig. S10 and S11. In pristine NMC and Gr electrodes, C–O & C═O components are observed from conductive carbon additives.[38] In contrast, D-NMC and D-Gr show a notable increase in C–O & C═O species and the emergence of Li–F, Li–O–C, and $Li_xPF_yO_z$ compounds, reflecting the accumulation of both organic and inorganic EEI components on the electrodes.[39,40] Following three CV scans, the R-NMC and R-Gr electrodes exhibit XPS spectra similar to pristine NMC and Gr, except for minor residual LiF, which strongly suggests the successful removal of most EEI species. The persistence of LiF is attributed to its chemical stability originating from a high ionic migration barrier of 0.729 eV and a large bandgap of ~13.6 eV.[41,42] Nonetheless, residual LiF can contribute positively by reinforcing structural stability and mitigating further interphase growth.[43,44] In the Li 1s and F 1s XPS spectra of D-NMC, R-NMC, D-Gr, and R-Gr, all organic and inorganic EEI components disappear after regeneration, leaving only LiF on both R-NMC and R-Gr (Fig. 2e and f). XPS depth profiling of electrodes before and after regeneration further demonstrates effective EEI removal. (Fig. 2g and h) While D-NMC shows progressive changes in its depth profiles of Li, C, O, and F and approaches the composition of pristine NCM during Ar^+ sputtering etching, R-NMC maintains consistent depth profiles during etching, representing the removal of the EEI layer from R-NMC. Similar behavior is observed for the Gr anode, where D-Gr shows substantial compositional changes during Ar^+ etching, whereas R-Gr maintains a stable depth profile. These results indicate that R-NMC and R-Gr show clean surfaces nearly identical to pristine electrodes because of the removal of the thick EEI layers during DEER. Finally, high-resolution transmission electron microscopy (HR-TEM) images of R-NMC and R-Gr further reveal clean active material surfaces identical to those of the pristine electrodes (Fig. 2i–l and Fig. S12). Whereas D-NMC and D-Gr exhibit thick EEI layers of approximately 10–20 nm and 30–40 nm, respectively, after prolonged cycling in carbonate electrolytes, these layers are completely absent in R-NMC and R-Gr. Multiple statistically meaningful TEM images of D-NMC and R-NMC are

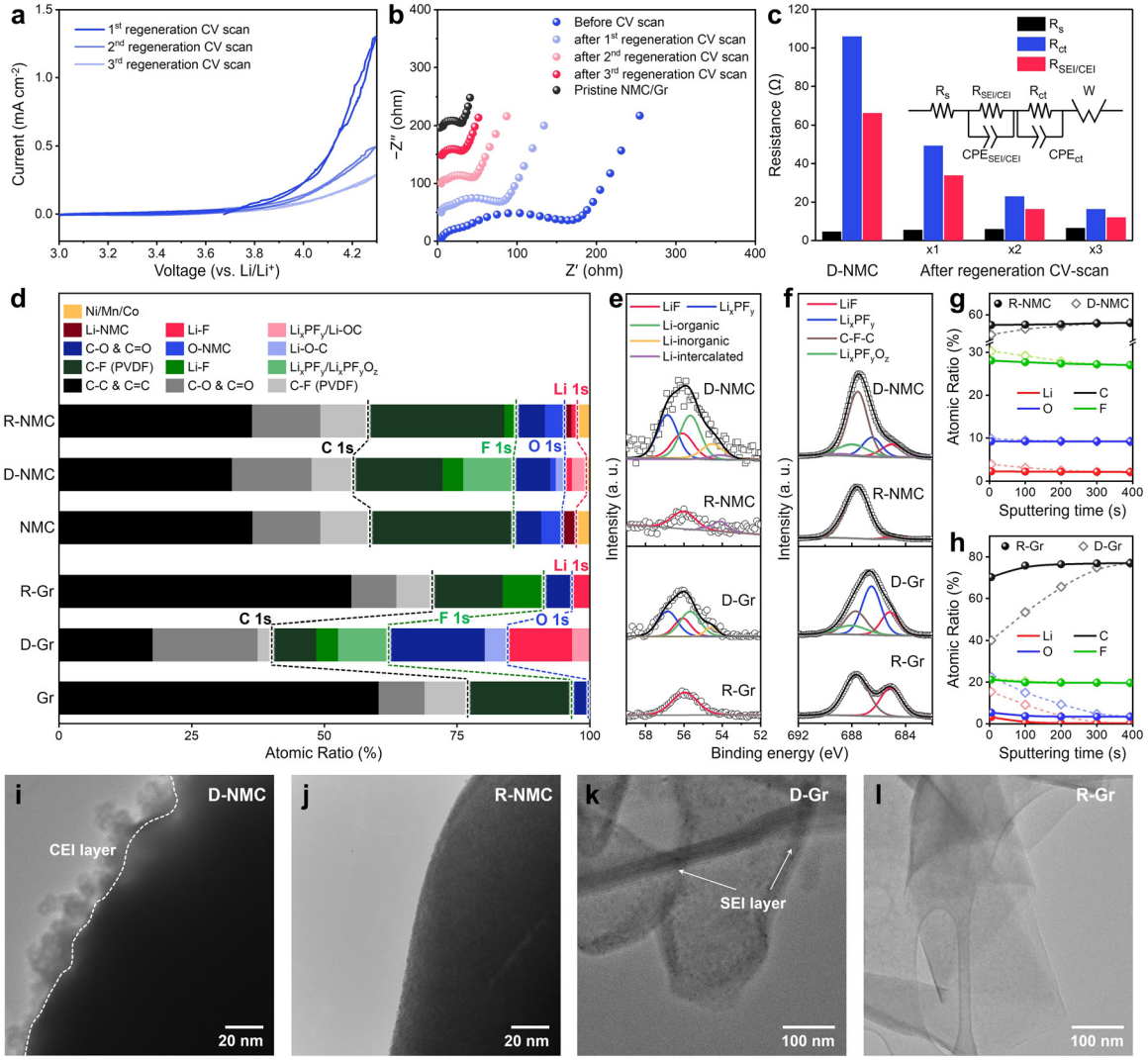

Fig. 2 (a) Cyclic voltammetry and (b) Nyquist plots of NMC/Gr and regenerated cells assembled with D-NMC/D-Gr, which are measured at OCV in the DMI electrolyte during the DEER regeneration scan. (c) The fitted results of R_s, R_{ct}, and R_{EEI} corresponding to the measured Nyquist plots and the c-inlet) equivalent circuit model for EIS fitting. (d) Relative comparison of the elemental compositions (atom%) and the corresponding (e) XPS Li 1s and (f) F 1s spectra of pristine NMC, D-NMC, R-NMC, pristine Gr (graphite), D-Gr, and R-Gr. Color coding of (d) was standardized as follows: C 1s as black, F 1s as green, O 1s as blue, Li 1s as red, and Ni/Mn/Co 2p as yellow. XPS depth profiles of (g) R-NMC and D-NMC under an Ar^+ ion energy of 1 keV with monoatomic mode, and (h) R-Gr and D-Gr under Ar^+ ion energy of 3.5 keV with monoatomic mode. HR-TEM images of (i) D-NMC, (j) R-NMC, (k) D-Gr, and (l) R-Gr before/after electrochemical recycling in DMI-electrolytes. Cathode-electrolyte interphase (CEI) from NMC and solid-electrolyte interphase (SEI) from graphite are considered as the EEI layer.

shown in Fig. S13 and S14. In addition, HR-SEM images of R-Gr further represent the clean and exposed graphite morphology comparable to those of pristine Gr (Fig. S15 and S16). D-NMC and D-Gr simply soaked in the DMI electrolyte without electrochemical DEER treatment or with only one CV scan during DEER show partial dissolution of the EEI layer but incomplete removal (Fig. S17 and S18). Although the lattice fringes of R-NMC and R-Gr exhibit subtle phase mixing and lattice distortion by battery cycling, the bulk crystal structures are largely preserved, which further suggests that electrode passivation by the EEI in used NMC/Gr cells is a major contributor to performance degradation (Fig. S19). Moreover, the unchanged XRD patterns of NMC and Gr after DEER, with the preserved electrode thickness observed by SEM, indicate that both the active materials and electrode architecture remain intact during the electrochemical EEI dissolution process (Fig. S20 and S21). Taken together, R-NMC and R-Gr treated by DEER show no apparent passivation layers, confirming not only successful EEI dissolution but also the absence of additional layer formation induced by the DMI-based electrolyte.

To validate the performance of the regenerated electrodes by DEER, the cycling stability and rate capabilities of R-NMC and R-Gr electrodes are evaluated in half-cell and full-cell configurations. All cells were reassembled using EC/DEC (1 : 1 v/v) with 1 M $LiPF_6$ as the electrolyte, keeping all components identical except for the electrodes. NMC/Gr refers to the cell fabricated with pristine NMC and Gr. R-NMC/Gr denotes the

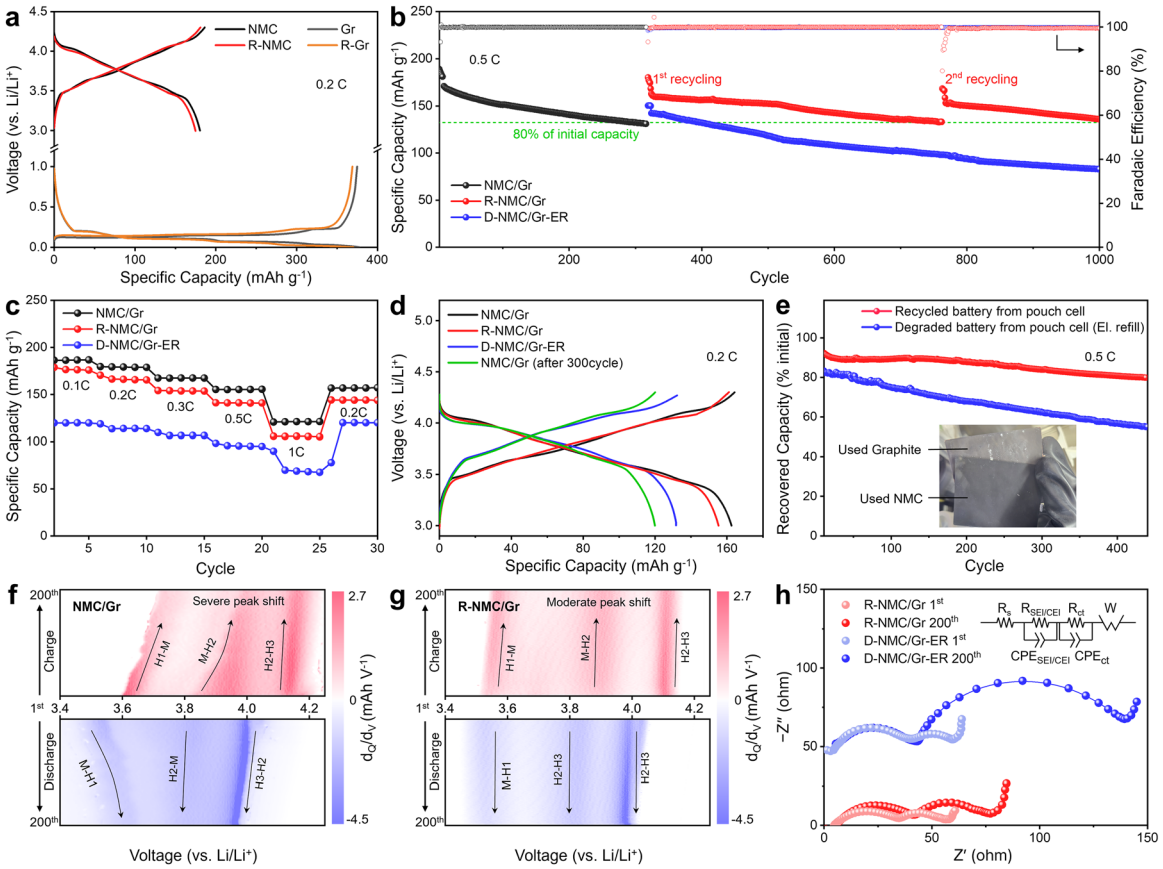

Fig. 3 (a) Voltage profiles of R-NMC and R-Gr in half-cell evaluation with the Li metal. (b) Electrochemical cycle performance, (c) rate capability measurements, and (d) discharge and charge curves of pristine NMC/Gr, R-NMC/Gr, and D-NMC/Gr-ER (no DEER treatment and only electrolyte refill). (e) The cycle performance of recycled batteries from commercial-scale pouch cells after DEER treatment. The d_Q/d_V profiles of (f) NMC/Gr and (g) R-NMC/Gr at 0.5C. (h) Nyquist plots of R-NMC/Gr and D-NMC/Gr at the 1st and 200th cycles, measured at 3.8 V in EC/DEC with 1 M $LiPF_6$ during cycling.

cell using R-NMC and R-Gr with fresh electrolyte, whereas D-NMC/Gr-ER (ER is the electrolyte refill) is the cell reassembled with D-NMC and D-Gr with fresh electrolyte but without DEER treatment. R-NMC and R-Gr with Li metal as the counter electrode after regeneration show capacities of 182.9 mAh g^{-1} at a 0.2C rate and 370.3 mAh g^{-1} at a 0.1C rate, respectively, which are 97% and 98% of the capacities of pristine NMR and Gr (Fig. 3a). The recovered capacities of R-NMC and R-Gr, relative to D-NMC and D-Gr, confirm that DEER recovers the EEI induced performance losses of both the cathode and anode. Half-cell EIS measurements further show that the increased resistance of D-NMC and D-Gr decreases to near pristine levels after DEER, confirming the effective removal of EEI-associated resistance (Fig. S22). In full cell evaluation, R-NMC/Gr shows a capacity of 162.9 mAh g^{-1} at a 0.5C rate after formation cycle, corresponding to 95% of its initial cell capacity. In contrast, capacity regain of only 83% of the original capacity is observed in D-NMC/Gr-ER, demonstrating that electrode passivation by the EEI was still a major contributor to performance degradation (Fig. 3b). Furthermore, after a second consecutive regeneration cycle, the third-life recycled battery exhibited 90% of its original capacity with 153.3 mAh g^{-1}, highlighting the repeatability of DEER to already regenerated electrodes. In addition, R-NMC/Gr exhibits a capacity of 0.042% of decay per cycle, which is 1.7 times lower than the 0.072% of D-NMC/ER, which is attributed to the presence of residual LiF. Extended cycling up to 1300 cycles shows that R-NMC/Gr shows an increased capacity decay rate of 0.067% per cycle after 800 cycles, indicating that reaccumulated EEI induces D-NMC/Gr-like fading behavior (Fig. S23). Thin LiF in the EEI layer is known to improve structural stability and suppress further EEI formation by limiting parasitic reactions.[45] The rate capability of R-NMC/Gr from 0.1C to 1C, comparable to that of NMC/Gr, reveals that Li^+ intercalation/deintercalation kinetics of R-NMC and R-Gr remain similar to pristine NMC and Gr electrodes, indicating that the active materials remained structurally and electrochemically intact (Fig. 3c and Fig. S24). Based on the almost identical charge/discharge voltage profiles and specific capacity between NMC/Gr and R-NMC/Gr, no kinetic loss or no electrode degradation occurs in R-NMC/Gr during DEER (Fig. 3d). To assess the feasibility of this approach under more practical conditions, we extended the DEER treatment to electrodes harvested from 3 Ah NMC811/Gr pouch cells after 2700 cycles of long-term degradation (Fig. S25). Following DEER treatment in a DMI-based electrolyte, the full cell with recycled commercial NMC and Gr electrodes shows a recovered capacity

of 166 mAh g^{-1}, which is approximately 90.3% of the initial specific capacity of NMC/Gr in 3 Ah pouch cells (Fig. 3e). Moreover, R-NMC/Gr from pouch cells shows more stable cycle performance compared to cells reassembled without DEER treatment. Although the harvested NMC and Gr electrodes were not regenerated at the full 3 Ah pouch cell scale, these results demonstrate that the DEER chemistry remains effective for commercially aged electrodes obtained from pouch cells. The slightly lower regained capacity compared to lab-scale cells can be attributed to deeper structural degradation in active materials, loss of reversible lithium, and the inevitable pre-processing and non-controlled disassembly in industrial settings. To further demonstrate the enhanced cycle performance of R-NMC/Gr after regeneration, the differential capacity analysis (d_Q/d_V) curves of D-NMC/Gr-ER and R-NMC/Gr are analyzed and plotted as a function of the cycle number (Fig. 3f and g, and Fig. S26). The d_Q/d_V analysis is particularly effective for identifying phase transition features and peak shifts linked to impedance evolution, enabling a clear evaluation of the electrochemical stability of the active materials over extended cycling.[46] In the first cycle, the H2–H3 discharge peak of R-NMC/GR appears at 3.99 V, lower than 4.05 V observed for NMC/Gr, consistent with residual LiF and minor degradation of the active materials (Fig. S26). Over long-term cycling, the d_Q/d_V profile of R-NMC/Gr exhibits minimal changes in the positions and intensities of the H1–M, M–H2, and H2–H3 peaks from the 1st to the 200th cycle, whereas NMC/Gr undergoes a pronounced shift for every peak. This peak shift in NMC/Gr observed during cycling, despite the use of fresh electrodes and electrolytes, underlines instability in interfacial redox behavior driven by the progressive accumulation of the inactive EEI species at the electrodes.[47,48] Moreover, the post-mortem XRD pattern of R-NMC after 200 cycles shows less crystal structure degradation and lattice shrinkage than that of D-NMC-ER, indicating that the residual LiF layer helps mitigate structural damage during cycling (Fig. S27 and S28). This LiF-driven interfacial stabilization is further confirmed by the higher faradaic efficiency (FE) of 99.94% of R-NMC as compared to the 99.76% of D-NMC/Gr-ER (Fig. 3b and Fig. S29). The remaining LiF on R-NMC/Gr stabilizes the electrode–electrolyte interface, facilitates charge transfer, and suppresses parasitic reactions, collectively enabling its improved cycling stability after DEER. The EIS of R-NMC/Gr further supports EEI dissolution after DEER treatment, as shown by the reduced R_{EEI} of 30 Ω for R-NMC/Gr relative to 36 Ω for D-NMC/Gr (Fig. 3h). After 200 cycles, however, the R_{CT} of D-NMC/Gr increases by 5-fold, indicating that cathode degradation is accelerated once the state-of-health falls below 80%. In contrast, the R-NMC/Gr cell shows only a 1.74-fold increase in R_{CT}, as the residual LiF with the removal of inactive EEI barriers effectively protects the electrode interface and helps maintain the structural integrity of the cathode.[37,49] Both the EIS and d_Q/d_V analyses demonstrate that regeneration not only recovers the capacity of end-of-life batteries but also enhances the long-term cycling stability of the regenerated electrodes.

To elucidate the fundamental mechanism of DMI-based recycling solutions in the DEER process, the *operando* Raman spectra of D-NMC and D-Gr electrodes were collected during the regeneration CV scan and presented as contour plots alongside the corresponding voltage profiles from 3.0 to 4.1 V *vs.* Li/Li^+ (Fig. 4a–c and Fig. S30 and S31). A custom-designed *operando* Raman cell was employed, in which all inactive cell components

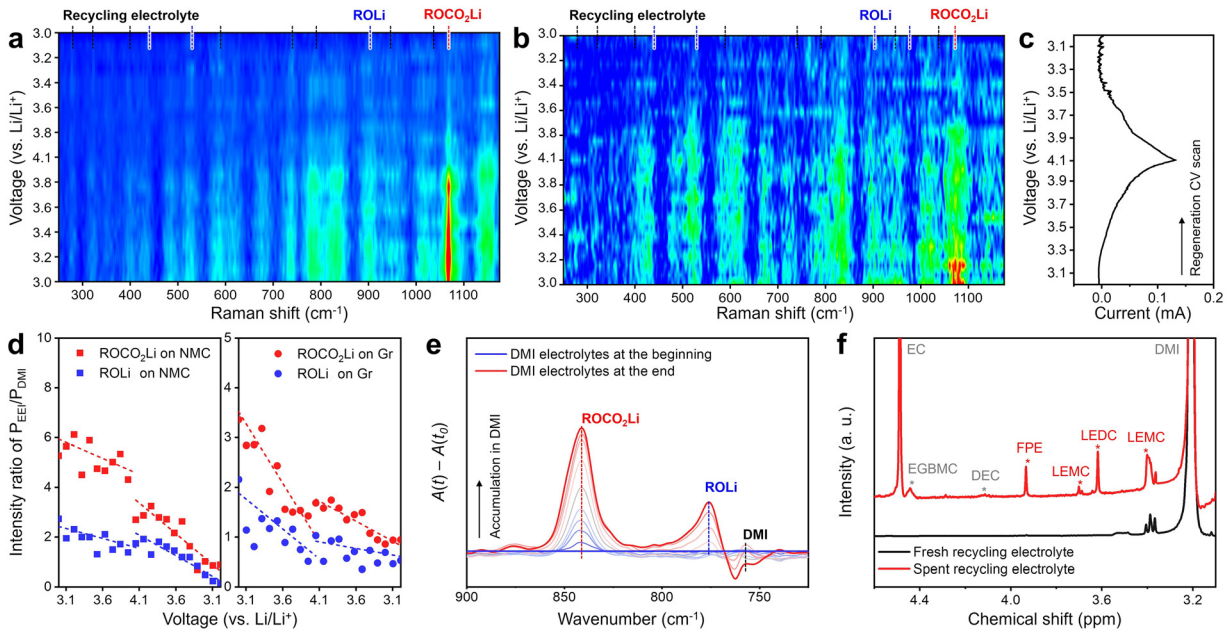

Fig. 4 The contour map for *operando* Raman spectra of (a) D-NMC and (b) D-Gr during DEER with EEI dissolution between 3.0 and 4.1 V *vs.* Li/Li^+. (c) The corresponding cyclic voltammogram curve for the Raman spectra. (d) The peak intensity ratio of the EEI peak of $ROCO_2Li$ at 1084 cm^{-1} and ROLi at 901 cm^{-1} over the DMI peak at 580 cm^{-1} for NMC and Gr during regeneration CV scan. (e) The *operando* IR spectra of the DMI recycling electrolyte during DEER treatment of D-NMC/Gr. (f) ^1H NMR spectra of fresh and spent DMI recycling electrolytes after DEER treatment of D-NMC/Gr.

were fabricated with ~1 mm holes to allow the laser to directly probe the degraded cathode or anode surfaces. Details of the cell configuration and measurement parameters are provided in Note S3. The pristine DMI electrolyte shows strong peaks at 581 and 786 cm^{-1} (Fig. S32). ROLi (RCOOLi) is identified at 433, 524, and 901 cm^{-1}, and $ROCO_2Li$ at 1072 cm^{-1}.[50,51] In the contour plots, peaks originating from the DMI recycling electrolyte are marked with black dotted lines, ROLi-related bands with blue dotted lines, and $ROCO_2Li$-related bands with red dotted lines. Although the Raman resolution of the Gr electrode is lower due to its higher carbon content and optical absorption, both electrodes exhibit similar ROLi and $ROCO_2Li$ features located at nearly identical positions, consistent with the fact that these EEI components primarily arise from the decomposition of carbonate electrolytes. Notably, $ROCO_2Li$ shows a stronger initial intensity than ROLi, reflecting its relatively simple formation pathway and chemical instability, which agrees with previous reports that suggest that $ROCO_2Li$ formation dominates under 0.1–0.5 C cycling conditions.[26] This similarity of EEI species and their relative composition confirms that the EEI of D-NMC and D-Gr resembles that of typical spent battery electrodes. The contour plots reveal a gradual fading of the $ROCO_2Li$ and ROLi bands as the regeneration CV scan progress, demonstrating the disappearance of EEI-related species from both electrode surfaces. For the NMC electrode, a prominent decrease in peak intensity is observed during the cathodic sweep from 4.1 to 3.0 V, whereas the Gr electrode exhibits more substantial changes during the anodic sweep from 3.0 to 4.1 V. These spectral evolutions closely correlate with the increase in current between 3.4 and 4.1 V in the CV profile, indicating that the dissolution of ROLi and $ROCO_2Li$ is electrochemically driven rather than purely chemical. Meanwhile, the overall intensity of the DMI-related peaks also slightly decreases with cycling, attributed either to the formation of solvation structures between DMI and dissolved EEI species or to minor autofocus fluctuations inherent to *operando* Raman measurement. Collectively, these results demonstrate that the EEI layer components continuously dissolve into the DMI medium during regeneration, confirming the electrochemical EEI dissolution mechanism during DEER.

To quantify these spectral changes, the intensity ratios of $ROCO_2Li$ at 1072 cm^{-1} and ROLi at 901 cm^{-1} (P_{EEI}) relative to the electrolyte reference peak at 786 cm^{-1} (P_{DMI}) were plotted as a function of DEER progression and the corresponding potential (Fig. 4d). The ratios of $ROCO_2Li$ and ROLi on NMC exhibit a monotonic decline from around 6 and 2, respectively, reaching less than 12% and 17% of their initial values after DEER, confirming the gradual elimination of organic EEI species from the NMC surface. A comparable trend is observed for the Gr electrode, where intensity ratios of P_{EEI} over P_{DMI} decrease by approximately 27% during DEER, indicating that EEI components on the Gr anode side are dissolving simultaneously with the dissolution of the EEI at the NMC cathode. In addition, although the P_{EEI}/P_{DMI} ratio gradually decreases throughout the entire regeneration CV scan, the decline in the P_{EEI}/P_{DMI} at the NMC electrode proceeds more rapidly during the cathodic sweep, whereas the decrease of P_{EEI}/P_{DMI} on the Gr is more prominent during the anodic sweep. This behavior suggests that small amount of organic EEI components can be chemically dissolved in the DMI electrolyte, while electrochemical reactions further accelerate their dissolution at specific potential regions and sweep. This observation is consistent with our finding that simple immersion of D-NMC and D-Gr in the DMI recycling electrolyte restores only about 90% capacity of R-NMC/Gr, indicating that chemical dissolution results in only partial EEI removal and that electrochemical protocol is required (Fig. S4). The *operando* Raman spectra of D-NMC and D-Gr during DEER provides direct evidence that the EEI layers are continuously dissolved into the DMI electrolyte electrochemically or chemically. Moreover, the distinct decline trends of EEI peaks on both electrodes represent potential-dependent dissolution of EEI species in the DMI medium.

To monitor the EEI species dissolved from the electrodes during DEER, *in-operando* attenuated total reflection Fourier-transform infrared (ATR-FTIR) spectroscopy was performed using a custom-designed coin-cell setup developed in our laboratory.[52] Compared with Raman spectroscopy, IR spectroscopy possesses a greater penetration depth of radiation with 2.03 μm at 1000 cm^{-1} and a larger spot size of 1.5 mm, enabling comprehensive detection capability of newly formed or dissolved species in the electrolyte. To ensure that only the electrolyte region was probed during cell operation, a window of approximately 2 mm diameter, larger than the sampling area of the ATR crystal, was introduced at the electrodes (Note S3). This configuration allowed the IR beam to interact exclusively with the electrolyte, minimizing interference from the electrode surface. To sensitively capture the minute dissolution behavior of EEI components, the absorbance variation, $A(t) - A(t_0)$, was analyzed over three consecutive CV scans, with the pristine DMI electrolyte spectrum shown for reference in Fig. S33.[53] As illustrated in Fig. 4e, the characteristic peaks at 841 cm^{-1} and 776 cm^{-1}, corresponding to $ROCO_2Li$ and ROLi, respectively, gradually increase in intensity during regeneration, indicating their accumulation in the electrolyte.[26] The $ROCO_2Li$ signal rises more rapidly than ROLi at an early stage of DEER treatment, consistent with the earlier observation that $ROCO_2Li$ is more abundant on both cathode and anode surfaces and chemically less stable than ROLi. In contrast, the DMI band at 758 cm^{-1} exhibits negligible intensity variation during regeneration, suggesting that DMI itself neither decomposes nor participates in parasitic reactions with EEI constituents. This observation shows that the EEI interphase dissolution is governed by an electrochemical solvation-driven mechanism enabled by the high donor number and strong coordinating ability of DMI.

To identify the species dissolved into the DMI recycling solution, the ^1H nuclear magnetic resonance (NMR) spectra of fresh and used DMI electrolytes were measured (Fig. 4f). The fresh DMI electrolyte exhibits characteristic peaks at 2.5 and 3.2 ppm, corresponding to the intrinsic proton signals of DMI, while the solvent DMSO shows resonances at 2.5 ppm (Fig. S34).[54] The conventional EC/DEC-based electrolyte displays strong carbonate-derived peaks at 4.49 and 4.11 ppm (Fig. S34), which are also detected in the used DMI electrolyte, attributed to the trace EC and DEC residues originally adsorbed on the D-NMC and D-Gr electrodes. Notably, the used DMI electrolyte exhibits new peaks at 3.41,

3.61, 3.69, 3.93, and 4.41 ppm, which are assigned to dissolved EEI species classified as $ROCO_2Li$ and ROLi families, including lithium ethylene di-carbonate (LEDC), lithium ethylene mono-carbonate (LEMC), fluorophosphate ester (FPE, $OPF_2(OCH_3)$) and ethylene glycol bis-methyl carbonate (EGBMC) originating from the catalytic reaction of $LiPF_6$ and EC/DEC during battery cycling.[40,55,56] The peaks of EEI are clearly distinguishable from those of EC and DEC and match well with previously reported EEI component resonances. This agreement confirms that EEI species on both NMC and Gr do not decompose in the DMI solution but instead dissociate through the formation of stable solvation structures. Moreover, possible cross contamination was examined by ^{1}H NMR analysis of R-NMC and R-Gr after DEER, confirming negligible residual soluble species on both regenerated electrodes (Fig. S35). The observation of accumulated carbonate-derived species such as $ROCO_2Li$ and ROLi in the used DMI electrolytes, identified by *operando* FTIR and NMR, indicates that the high donor number and strong solvation capability of DMI drive effective EEI dissolution during DEER.

Following the establishment of the capacity regain of R-NMC/Gr and the EEI dissolution mechanism of DEER, we next assess its economic and environmental viability. As illustrated in Fig. 5a, DEER has significantly fewer steps than the pyrometallurgical (pyro), hydrometallurgical (hydro), and direct battery recycling processes by eliminating the need for shredding, mechanical disassembly, thermal treatment, materials leaching, materials synthesis, chemical treatment for recycling, and battery manufacturing processes, including electrode fabrication. The DEER treatment does not require the extensive preprocessing needed to produce black mass for hydro and direct recycling (Fig. S36), as well as the detailed equipment and process sequence of DEER are much simpler than other recycling routes (Fig. S37–S39). After DEER, the regenerated electrodes from the end-of-life batteries can be directly reintegrated into the battery manufacturing process.

To evaluate the practical feasibility of the developed DEER, technoeconomic (TEA) and life-cycle environmental analyses (LCA) were conducted and compared with pyro- and hydro-recycling routes. The EverBatt2023 model developed by Argonne National Laboratory was employed to compare different recycling pathways.[57] A detailed description of the methodology, including the assumptions and modifications applied in this study, is provided in Note S4. The total cost of DEER per kg of feedstock of end-of-life NMC811 cells is 4.50 \$ per kg_{feed}, which is slightly higher than 3.87 \$ per kg_{feed} for pyro and 3.82 \$ per kg_{feed} for hydro (Fig. 5b). This is primarily because the cost of the DMI recycling electrolyte accounts for approximately 63% of the overall DEER cost (Fig. S40 and Table S2). However, DEER yields 14.34 \$ per kg_{feed}, nearly triple the revenue of pyro- and hydro-metallurgical processes due to its direct production of regenerated NMC cathodes and Gr anodes rather than Li, Ni, and Co precursors. Therefore, despite its higher recycling cost by DMI recycling electrolyte, DEER shows a profit of 9.84 \$ per kg_{feed}, outperforming the 1.22 and 2.11 \$ per kg_{feed} of pyro and hydro,

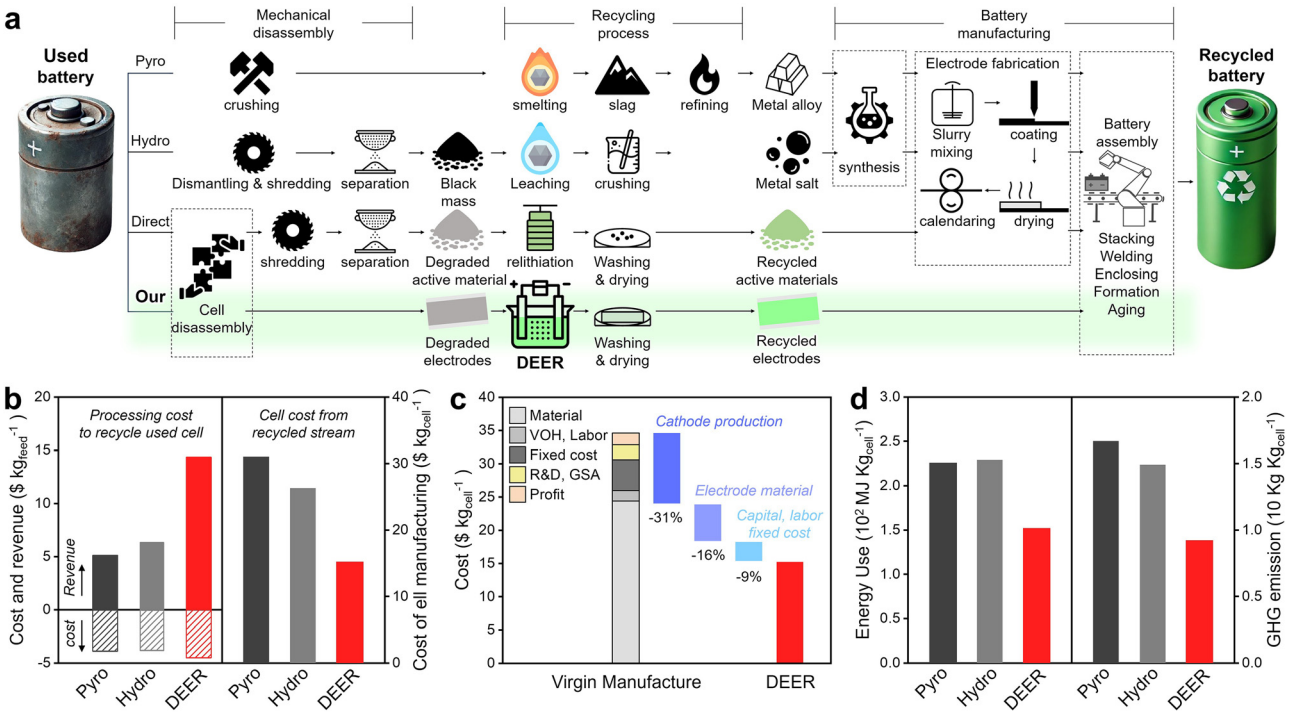

Fig. 5 Environmental and economic impacts of conventional, direct, and our intact battery recycling technologies. (a) Process flow diagrams of various spent lithium-ion battery recycling routes. (b) The cost and revenue analysis for the recycling process per kg of end-of-life NMC811 cells and the cost for manufacturing per kg of recycled cell *via* pyro, hydro, and DEER. (c) Breakdown of costs for recycled cell manufacturing through DEER based on cathode materials, electrode materials, and the electrode fabrication process. (d) Energy uses and GHG emission in manufacturing per kg of recycled cell *via* pyro, hydro, and DEER. Pyro: pyrometallurgical method, hydro: hydrometallurgical method, and GHG: greenhouse gas.

respectively, and offering better economic viability (Fig. S41). Beyond the cost and revenue of feedstock recycling, the cell manufacturing cost was further analyzed to assess the economic benefits of using regenerated NMC and Gr electrodes. The cost of cell manufacturing *via* DEER is 15.25 \$ per kg_{cell}, resulting in approximately 50% lower cost than the cost of pyro- (26.31 \$ per kg_{cell}) and hydro-based (31.07 \$ per kg_{cell}) recycling routes due to the simplicity of the DEER process, operated at room temperature, together with the elimination of material synthesis and electrode manufacturing steps (Fig. 5b and Table S3). The cost breakdown of cell manufacturing *via* DEER reveals that this reduction originates from 31% in cathode production, 16% from electrode-material savings including current collectors, binders, and solvents, and 9% from fixed costs such as capital and labor associated with electrode manufacturing, compared to conventional virgin battery manufacturing (Fig. 5c and Tables S4 and S5). In addition, the total energy consumption of DEER, 152 MJ kg_{cell}^{-1}, is about 34% lower than those of the pyro and hydro routes. Compared with pyro- and hydro-based recycling, the DEER route delivers substantially lower climate-related impacts, reducing harmful air pollutants and using considerably less water than both virgin battery manufacturing and conventional pyro/hydro recycling approaches (Fig. S42). Therefore, the DEER route yields competitive recycling profits, and enables less carbon/energy circularity, demonstrating its potential viability in the future battery recycling industries. Additionally, we note that 63% of the DEER cost is attributed to the cost of DMI recycling electrolytes and the current calculations do not include solvent recovery, which would save additional cost. With further development and optimization, this solvent cost may be further reduced by either using cheaper alternatives and/or recycling the solvent (Fig. S40 and S43 and Table S4). We evaluated intact-cell DEER by injecting the DMI electrolyte into a custom coin cell without disassembly, but direct cycling after treatment showed poor performance (Fig. S44). The capacity was recovered only after washing and reassembly with fresh LP40, suggesting that future intact cell DEER will require a system that enables an outlet for the recycling solvent followed by injection of the electrolyte. Furthermore, we propose scalable DEER designs for pouch and prismatic cells, including a custom flow-based intact pouch cell platform and a conceptual cell architecture for future treatment without disassembly (Fig. S45). Together with an envisioned grid energy storage system incorporating controlled electrolyte circulation and removal, these designs highlight the potential of DEER for in place regeneration of large format battery systems.

Conclusion

This work establishes an electrochemical recycling strategy, DEER, that directly restores end-of-life lithium ion battery electrodes by dissolving the accumulated EEI layers. By dissolving inactive EEI components through electrochemical activation in a high donor number environment, DEER regenerates both NMC cathodes and graphite anodes up to 95% of its initial capacity while bypassing conventional electrode manufacturing steps. *Operando* spectroscopy and surface analyses show that regeneration is governed by interfacial accessibility rather than irreversible material degradation over a wide range of practical states of health. TEA and LCA of DEER indicate lower recycled cell manufacturing cost and energy demand relative to pyro and hydro routes, primarily by bypassing material re-synthesis and electrode fabrication. Importantly, this work shifts the paradigm of battery recycling from material reconstruction toward electrode regeneration without complicated processes to generate black mass powder *via* shredding and dismantling. By enabling electrodes harvested from truly end-of-life batteries to be directly regenerated and reused, DEER establishes electrode–electrolyte interphase engineering as a foundational design principle for next-generation battery recycling.

Author contributions

Conceptualization: K. K. and V. K. Methodology: K. K. Investigation: K. K. and C. Y. Visualization: K. K. Software: C. Y., S. Y., and S. G. Supervision: V. K. Writing – original draft: K. K. Writing – review & editing: K. K. and V. K.

Conflicts of interest

There are no conflicts of interest to declare.

Data availability

All data supporting the findings of this study are available within the paper and its supplementary information (SI). Supplementary information: additional experimental details, simulation procedures, *operando* analyses, life-cycle assessment (LCA) and techno-economic analysis (TEA), as well as extended results and discussions. See DOI: https://doi.org/10.1039/d6ee01118g.

Source data are provided with this paper, and additional data are available from the corresponding authors upon reasonable request.

Acknowledgements

This project was supported by the Cornell Atkinson Center for Sustainability and PI's Pao-Wang Fellowship (Cornell University). We also acknowledge the use of shared facilities and resources provided by the Cornell Center for Materials Research (CCMR). Techno-economic and life-cycle assessments in this work were conducted using EverBatt, a techno-economic analysis and life-cycle assessment tool developed at the U.S. Department of Energy (DOE) ReCell Center for Advanced Battery Recycling, at Argonne National Laboratory. The ReCell Center is fully supported by the DOE Transportation Technology office (TTO). The spent NMC and graphite electrode sheets from pouch cells are provided by Charge CCCV, C4V (New York, US). We further thank Tran Ngo, Jantakan Nedsaengtip, and Samia Rahman for their assistance with the analysis of XRD, SEM, *operando* FTIR and Raman measurement.

References

1 H. Li, A. Berbille, X. Zhao, Z. Wang, W. Tang and Z. L. Wang, *Nat. Energy*, 2023, **8**, 1137–1144.
2 M. Zhai, Y. Wu, S. Tian, H. Yuan, B. Li, X. Luo, G. Huang, Y. Fu, M. Zhu and Y. Gu, *Nature*, 2025, 1–8.
3 Y. Feng, Y. Park, S. Hao, C. Qiu, S. Zhang, Z. Yu, Z. Fang, T. Terlier, C. Sellers and K. Mateen, *Joule*, 2025, **9**(12), 102197.
4 P. Zhu, Z. Jiang, W. Sun, Y. Yang, D. S. Silvester, H. Hou, C. E. Banks, J. Hu and X. Ji, *Energy Environ. Sci.*, 2023, **16**, 3564–3575.
5 R. E. Ciez and J. Whitacre, *Nat. Sustainability*, 2019, **2**, 148–156.
6 L. L. Driscoll, A. Jarvis, R. Madge, E. H. Driscoll, J.-M. Price, R. Sommerville, F. S. Tontini, M. Bahri, M. Miah and B. L. Mehdi, *Joule*, 2024, **8**, 2735–2754.
7 Z. Zhuang, J. Li, H. Ji, Z. Piao, X. Wu, G. Ji, S. Liu, J. Ma, D. Tang and N. Zheng, *Adv. Mater.*, 2024, **36**, 2313144.
8 M. Yoon, J.-S. Park, W. Chen, Y. Huang, T. Dai, Y. Lee, J. Shin, S. Lee, Y. Kim and D. Lee, *Energy Environ. Sci.*, 2025, **18**, 5902–5912.
9 Z. Liu, M. Han, S. Zhang, H. Li, X. Wu, Z. Fu, H. Zhang, G. Wang and Y. Zhang, *Adv. Mater.*, 2024, **36**, 2404188.
10 J. Ma, J. Wang, K. Jia, Z. Liang, G. Ji, H. Ji, Y. Zhu, W. Chen, H.-M. Cheng and G. Zhou, *Nat. Commun.*, 2024, **15**, 1046.
11 H. Zhang, Y. Ji, Y. Yao, L. Qie, Z. Cheng, Z. Ma, X. Qian, R. Yang, C. Li and Y. Guo, *Energy Environ. Sci.*, 2023, **16**, 2561–2571.
12 M. Xu, C. Wu, L. Ye, Y. Zhang, C. Zhang, J. Hu, R. Tan, D. Gu, X. Wang and O. Fontaine, *Adv. Energy Mater.*, 2024, **14**, 2401197.
13 Y. Liu, R. Zhang, J. Wang and Y. Wang, *IScience*, 2021, **24**(4), 102332.
14 S. Ko, J. Choi, J. Hong, C. Kim, U. Hwang, M. Kwon, G. Lim, S. S. Sohn, J. Jang and U. Lee, *Energy Environ. Sci.*, 2024, **17**, 4064–4077.
15 N. Ogihara, K. Nagaya, H. Yamaguchi, Y. Kondo, Y. Yamada, T. Horiba, T. Baba, N. Ohba, S. Komagata and Y. Aoki, *Joule*, 2024, **8**, 1364–1379.
16 M. Zheng, Y. You and J. Lu, *Nat. Rev. Mater.*, 2025, 1–14.
17 W. Guo, Z. Sun, J. Guo, Y. Li, S. B. Vilsen and D. I. Stroe, *Adv. Energy Mater.*, 2024, **14**, 2401644.
18 C. R. Birkl, M. R. Roberts, E. McTurk, P. G. Bruce and D. A. Howey, *J. Power Sources*, 2017, **341**, 373–386.
19 M. Li, X. Yang, X. Wei, Y. Zhu, X. Sun and M. D. Gu, *Nano Lett.*, 2025, **25**, 2769–2776.
20 Y.-S. Li, Y.-L. Ye, Z.-X. Xie, X.-D. Zhang, X.-S. Zhang, C.-H. Ke, Z.-H. Zhang, R. Wen, H. Yang and H. Ye, *J. Am. Chem. Soc.*, 2025, **147**, 36244–36253.
21 J. Xiao, N. Adelstein, Y. Bi, W. Bian, J. Cabana, C. L. Cobb, Y. Cui, S. J. Dillon, M. M. Doeff and S. M. Islam, *Nat. Energy*, 2024, **9**, 1463–1473.
22 M. Goktas, C. Bolli, E. J. Berg, P. Novák, K. Pollok, F. Langenhorst, M. V. Roeder, O. Lenchuk, D. Mollenhauer and P. Adelhelm, *Adv. Energy Mater.*, 2018, **8**, 1702724.
23 C. Kirwa, E. Wang, S. B. Son, J. Preimesberger, F. D. Key, Y. Bai, K. Pupek, H. Luo, M. Keyser and J. Coyle, *Adv. Energy Mater.*, 2025, 2501809.
24 T. Ouaneche, L. Stievano, L. Monconduit, C. Guèry, N. Recham and M. T. Sougrati, *EES Batteries*, 2025, **1**, 1068–1082.
25 E. J. McShane, H. K. Bergstrom, P. J. Weddle, D. E. Brown, A. M. Colclasure and B. D. McCloskey, *ACS Energy Lett.*, 2022, **7**, 2734–2744.
26 H. Lv, L. Zhou, Q. Fang, J. Cheng, J. Mei, Y. Xia and B. Wang, *Small*, 2024, **20**, 2312204.
27 J. Xu, J. Zhang, T. P. Pollard, Q. Li, S. Tan, S. Hou, H. Wan, F. Chen, H. He and E. Hu, *Nature*, 2023, **614**, 694–700.
28 V. Gutmann, *Electrochim. Acta*, 1976, **21**, 661–670.
29 P. Zhou, Y. Xiang and K. Liu, *Energy Environ. Sci.*, 2024, **17**, 8057–8077.
30 S. Liu, X. Ji, N. Piao, J. Chen, N. Eidson, J. Xu, P. Wang, L. Chen, J. Zhang and T. Deng, *Angew. Chem., Int. Ed.*, 2021, **60**, 3661–3671.
31 D. Wu, Y. Z. Wang, G. L. Zhang, X. Y. Chen, P. Cui and H. J. Feng, *Small*, 2024, **20**, 2307945.
32 M. Baek, H. Shin, K. Char and J. W. Choi, *Adv. Mater.*, 2020, **32**, 2005022.
33 P. Zhou, Y. Xiang and K. Liu, *Energy Environ. Sci.*, 2024, **17**, 8057–8077.
34 Q. Ma, S. Fu, A. J. Wu, Q. Deng, W. D. Li, D. Yue, B. Zhang, X. W. Wu, Z. L. Wang and Y. G. Guo, *Adv. Energy Mater.*, 2023, **13**, 2203892.
35 M. Zhou, P. Bai, X. Ji, J. Yang, C. Wang and Y. Xu, *Adv. Mater.*, 2021, **33**, 2003741.
36 Y. Zhang, Y. Katayama, R. Tatara, L. Giordano, Y. Yu, D. Fraggedakis, J. G. Sun, F. Maglia, R. Jung and M. Z. Bazant, *Energy Environ. Sci.*, 2020, **13**, 183–199.
37 J. Guo, S. Jin, X. Sui, X. Huang, Y. Xu, Y. Li, P. K. Kristensen, D. Wang, K. Pedersen and L. Gurevich, *J. Mater. Chem. A*, 2023, **11**, 41–52.
38 Y. Chen, W. Zhao, Q. Zhang, G. Yang, J. Zheng, W. Tang, Q. Xu, C. Lai, J. Yang and C. Peng, *Adv. Funct. Mater.*, 2020, **30**, 2000396.
39 L. Chen, Q. Nian, D. Ruan, J. Fan, Y. Li, S. Chen, L. Tan, X. Luo, Z. Cui and Y. Cheng, *Chem. Sci.*, 2023, **14**, 1184–1193.
40 Y.-F. Tian, S.-J. Tan, C. Yang, Y.-M. Zhao, D.-X. Xu, Z.-Y. Lu, G. Li, J.-Y. Li, X.-S. Zhang and C.-H. Zhang, *Nat. Commun.*, 2023, **14**, 7247.
41 D. Roessler and W. Walker, *J. Phys. Chem. Solids*, 1967, **28**, 1507–1515.
42 Y. Chen, C. Ouyang, L. Song and Z. Sun, *J. Phys. Chem. C*, 2011, **115**, 7044–7049.
43 Y. Lu, Z. Tu and L. A. Archer, *Nat. Mater.*, 2014, **13**, 961–969.
44 B. P. Thapaliya, T. Wang, A. Y. Borisevich, H. M. Meyer III, X. G. Sun, M. P. Paranthaman, C. A. Bridges and S. Dai, *Adv. Funct. Mater.*, 2023, **33**, 2302443.
45 P. Bai, X. Ji, J. Zhang, W. Zhang, S. Hou, H. Su, M. Li, T. Deng, L. Cao and S. Liu, *Angew. Chem., Int. Ed.*, 2022, **61**, e202202731.
46 B. Pei, H. Zhou, Y. Zong, X. Chen, M. J. Zuba, G. Zhou, H. Liu and M. S. Whittingham, *ACS Energy Lett.*, 2024, **9**, 3913–3921.
47 H. Ji, J. Wang, H. Qu, J. Li, W. Ji, X. Qiu, Y. Zhu, H. Ren, R. Shi and G. Ji, *Adv. Mater.*, 2024, **36**, 2407029.
48 Q. Zhang, Y. Chu, J. Wu, P. Dong, Q. Deng, C. Chen, K. Huang, C. Yang and J. Lu, *Adv. Energy Mater.*, 2024, **14**, 2303764.

49 G. Li, Z. Li, Q. Cai, C. Yan, L. Xing and W. Li, *ChemSusChem*, 2022, **15**, e202200543.
50 A. Gajan, C. Lecourt, B. E. Torres Bautista, L. Fillaud, J. Demeaux and I. T. Lucas, *ACS Energy Lett.*, 2021, **6**, 1757–1763.
51 E.-M. You, Y. Gu, J. Yi, D.-Y. Wu, J.-F. Li and Z.-Q. Tian, *Electrochim. Acta*, 2024, **498**, 144689.
52 T. Yim, R. Pereira, J. Nedsaengtip, A. T. Fafarman and V. Kalra, *J. Phys. Chem. Lett.*, 2024, **15**, 12164–12170.
53 C. Leau, Y. Wang, C. Gervillié-Mouravieff, S. T. Boles, X.-H. Zhang, S. Coudray, C. Boussard-Plédel and J.-M. Tarascon, *Nat. Commun.*, 2025, **16**, 757.
54 Z. Huang, J. Meng, W. Zhang, Y. Shen and Y. Huang, *Sci. Bull.*, 2022, **67**, 141–150.
55 L. Wang, A. Menakath, F. Han, Y. Wang, P. Y. Zavalij, K. J. Gaskell, O. Borodin, D. Iuga, S. P. Brown and C. Wang, *Nat. Chem.*, 2019, **11**, 789–796.
56 B. L. Rinkel, J. P. Vivek, N. Garcia-Araez and C. P. Grey, *Energy Environ. Sci.*, 2022, **15**, 3416–3438.
57 Q. Dai, J. Spangenberger, S. Ahmed, L. Gaines, J. C. Kelly and M. Wang, *EverBatt: A closed-loop battery recycling cost and environmental impacts model*, Argonne National Laboratory (ANL), Argonne, IL (United States), 2019.

